Advanced Materials

ADVANCED MATERIALS
www.advmat.de

RESEARCH ARTICLE OPEN ACCESS

Solvent-Mediated Reactivity Control of Lewis-Paired Dopants as a Versatile Strategy for Tunable and Stable Doping of Organic Semiconductors

Sang Beom Kim[1] | Eui Hyun Suh[1] | Taek Seong Lee[1] | Andreas W. Erhardt[2] | Iain McCulloch[2,3] | Jaeyoung Jang[1]

[1]Department of Energy Engineering, Hanyang University, Seoul, Republic of Korea | [2]Department of Chemistry, University of Oxford, Oxford, UK | [3]Andlinger Center for Energy and the Environment and Department of Electrical and Computer Engineering, Princeton University, Princeton, New Jersey, USA

Correspondence: Jaeyoung Jang (jyjang15@hanyang.ac.kr)

Received: 8 November 2025 | **Revised:** 2 February 2026 | **Accepted:** 20 March 2026

Keywords: Lewis acid-base chemistry | molecular dopants | organic semiconductors | Seebeck coefficients | tunable doping

ABSTRACT

The Lewis pairing between existing dopant molecules offers great potential for developing new organic dopants with exceptional doping strength and stability. However, the high reactivity of Lewis-paired dopants complicates doping-level control, while the use of non-orthogonal solvents can damage organic semiconductor (OSC) films, hindering device applications. Here, the dopant reactivity is controlled by regulating the association–dissociation kinetics among pairing dopants and solvent molecules, which are strongly influenced by solvent polarity. In highly polar solvents, Lewis acid–solvent adducts predominantly form, suppressing the generation of Lewis-paired dopants. As solvent polarity decreases, the dissociation rate of the Lewis acid–solvent adduct increases, establishing a dynamic equilibrium between the Lewis acid and the solvent and thereby optimizing reactivity. Consequently, the optimally processed Lewis-paired dopant enables efficient doping of various OSCs with finely tunable doping levels, simultaneously achieving a high thermoelectric power factor (170 $\mu W\ m^{-1}\ K^{-2}$) and Seebeck coefficient (227 $\mu V\ K^{-1}$). These performances surpass those of the conventional salt-type $FeCl_3$ dopant and exhibit markedly improved doping stability under ambient and elevated-temperature conditions. This study provides a practical strategy for utilizing Lewis-paired dopants by elucidating their doping mechanisms, paving the way to overcome long-standing limitations in OSC doping.

1 | Introduction

Molecular doping is a key technique for modulating the optical and electrical properties of organic semiconductors (OSCs), which require finely tunable doping levels for applications in a wide range of devices [1–4]. In optoelectronic and photovoltaic devices, OSCs employed in transport layers should possess optimized energy levels to ensure Ohmic contact with adjacent layers and achieve high current densities [5–7]. In thermoelectric (TE) devices, maximizing the figure of merit requires precise control of the charge carrier concentration, typically within the range of 10^{19}–10^{21} cm^{-3} [8–10]. Therefore, the systematic fine-tuning of the doping level, rather than simply maximizing electrical conductivity, is of greater importance. However, only a few organic dopants are widely used, owing to the challenges faced in simultaneously achieving high doping strength, doping stability, and synthetic accessibility in a single design [11–17]. Effective doping of OSCs (e.g., p-type doping) requires dopant molecules with strong oxidizing ability to extract electrons from the host materials. Accordingly, the lowest unoccupied molecular orbital

---

Sang Beom Kim and Eui Hyun Suh contributed equally to this study.

Advanced Materials, 2026; 0:e22233
https://doi.org/10.1002/adma.202522233

(LUMO) level of the p-dopant should lie below the highest occupied molecular orbital (HOMO) level of the OSC, which typically ranges from −4.80 to −5.92 eV [1, 3, 18, 19].

We recently introduced Lewis-paired CN groups as a new class of building blocks for exceptionally strong and stable organic p-dopants [18]. Lewis pairing between various Lewis acids (LAs) and CN-functionalized conjugated molecules strengthens the electron-withdrawing properties of CN groups by nearly twofold, deepening their LUMO levels by 0.60–0.91 eV (down to −5.93 eV). Furthermore, the increased molecular size of the dopants effectively suppresses the migration of the dopant counterions, thereby resulting in remarkable doping stability [18, 20]. Despite these advantages, the use of Lewis-paired dopants remains challenging [21]. For instance, they are incompatible with solution-sequential processing (SqP)—a representative doping method that relies on dopant diffusion into precoated OSC films [22–28]. These dopants are more favorably formed in nonpolar solvents such as chlorobenzene (CB) or *o*-1,2-dichlorobenzene, which do not react with individual pairing components or the resulting paired dopant [18, 20]. Consequently, in such nonpolar media, the formation of Lewis-paired dopants is maximized. However, the OSC film can be either partially dissolved by the solvent at low dopant concentrations or over-doped at high dopant concentrations, thereby hindering precise control over the doping level [18, 29]. To address this issue, a thermal dedoping step (≈200°C) was implemented to adjust the doping levels to an optimal range. However, the electrical conductivity (σ) remained low (<13 S cm^{-1}) even after dedoping, as over-doping and partial dissolution by the nonpolar CB solvent irreversibly disrupted the structural ordering of the OSC films.

For effective doping without damaging the OSC layers via SqP, the dopant solvent must simultaneously satisfy three criteria: (1) sufficient solubility for the dopant, (2) orthogonality to prevent dissolution of OSC films, and (3) adequate wettability on the OSC surface to facilitate dopant infiltration [11, 23, 30, 31]. Accordingly, polar organic solvents such as acetonitrile (ACN) and acetone (Ace) have been widely employed for SqP [22, 24, 30]. However, these polar solvents strongly coordinate with LAs to form LA–solvent adducts [32, 33], which compete with the formation of Lewis-paired dopants and reduce overall doping efficiency. Interestingly, Zapata-Arteaga et al. recently reported σ values of up to 300 S cm^{-1} for OSC films doped with Lewis-paired dopants using polar solvents [34]. In that study, post-SqP heating (120°C) and subsequent ACN washing were required to activate Lewis-paired dopant formation and remove residual dopants. However, the complex role of solvent polarity in Lewis-paired dopant systems remains poorly understood because polar solvents not only form LA–solvent adducts but also tend to stabilize the produced Lewis-paired dopants [35, 36]. This raises unresolved questions about how solvent polarity governs the competition between the formation of LA–solvent adducts and Lewis-paired dopants. Therefore, to fully leverage the great potential of Lewis-paired dopants, it is crucial to understand how solvent polarity affects dopant reactivity during SqP, providing a foundation for processing strategies that allow precise control of doping levels without damaging OSC films.

Herein, we demonstrate that the reactivity of the Lewis-paired dopant 2,3-dichloro-5,6-dicyano-p-benzoquinone:tris (pentafluorophenyl)borane (DDQ:BCF) can be effectively controlled during SqP by regulating its association–dissociation kinetics, which are governed by solvent polarity. Six organic solvents with varying dielectric constants ($4.42 < \varepsilon_r < 35.9$) were employed as dopant solvents; these solvents dissolve both DDQ and BCF while exhibiting orthogonality to OSC films, except for CB. We observed that the doping efficiency of DDQ:BCF was strongly influenced by the dissociation rate of the BCF–solvent adducts. In the dopant solution, the equilibrium (BCF + solvent ⇌ BCF–solvent) initially shifted toward BCF–solvent adducts because of the large excess of the solvent. During solvent evaporation in SqP, these Lewis adducts dissociated more readily in less polar solvents, releasing free BCF to form DDQ:BCF pairs that induce p-doping in OSC films. BCF–ethyl acetate (EtOAc) dissociated more readily than BCF–ACN, resulting in higher doping efficiency and enabling optimal TE power factors (*PF*s) at lower dopant concentrations. Accordingly, processing with EtOAc effectively minimized the presence of unpaired dopants (DDQ and BCF), which disrupted molecular ordering and localized charge carriers. The DDQ:BCF doping with EtOAc could be applied to diverse OSCs, achieving a maximum *PF* of 170 μW m^{-1} K^{-2} with an exceptionally high Seebeck coefficient (*S*) of 227 μV K^{-1} at an optimal doping level.

2 | Results and Discussion

Among the series of Lewis-paired dopants reported in our previous study, DDQ:BCF was selected because it exhibited the deepest LUMO level (−5.93 eV) (Figure 1a) [18]. A total of seven conjugated polymers were employed as host OSCs (Figure S1); among them, poly[2,2′-[(2,5-bis(2-hexyldecyl)-3,6-dioxo-2,3,5,6-tetrahydro-pyrrolo[3,4-*c*]pyrrole-1,4-diyl)dithio-phene]-5,5′-diyl-*alt*-thiophen-2,5-diyl] (PDPP3T) was selected as the model OSC because of its highly planar backbone conformation and superior charge transport properties [37]. Furthermore, PDPP3T could not be doped with individual DDQ and BCF during SqP because of its deep HOMO level (−5.24 eV), while effective doping was achieved with their DDQ:BCF Lewis pair (Figure 1a; Figure S2). Figure 1b illustrates the competitive reaction among the DDQ, BCF, and solvent molecules in the dopant solution. To systematically evaluate the effects of solvent polarity on this competitive reaction, we selected six organic solvents covering a wide range of ε_r from 4.42 to 35.9: CB, diethyl ether (DEE), tetrahydrofuran (THF), EtOAc, Ace, and ACN. The DDQ:BCF solutions in these solvents were deposited onto spinning OSC films to induce SqP doping, as illustrated in Figure 1c. To understand this solvent-dependent competitive reaction, the underlying reaction framework of the DDQ:BCF doping system is described below in terms of a series of equilibria, where S denotes the solvent and P denotes the polymer.

$$\mathrm{BCF} + \mathrm{S} \rightleftharpoons \mathrm{BCF} - \mathrm{S} \rightarrow (k_1/k_{-1} = K_1) \tag{1}$$

$$\mathrm{DDQ} + \mathrm{BCF} \rightleftharpoons \mathrm{DDQ} - \mathrm{BCF} \rightarrow (k_2/k_{-2} = K_2) \tag{2}$$

$$\mathrm{DDQ} - \mathrm{BCF} + \mathrm{P} \rightleftharpoons \mathrm{P}^{+}:\ \mathrm{DDQ} - \mathrm{BCF}^{-} \rightarrow (k_3/k_{-3} = K_3) \tag{3}$$

This series of equilibria provides the theoretical basis for the subsequent discussion of the solvent-dependent doping mechanism.

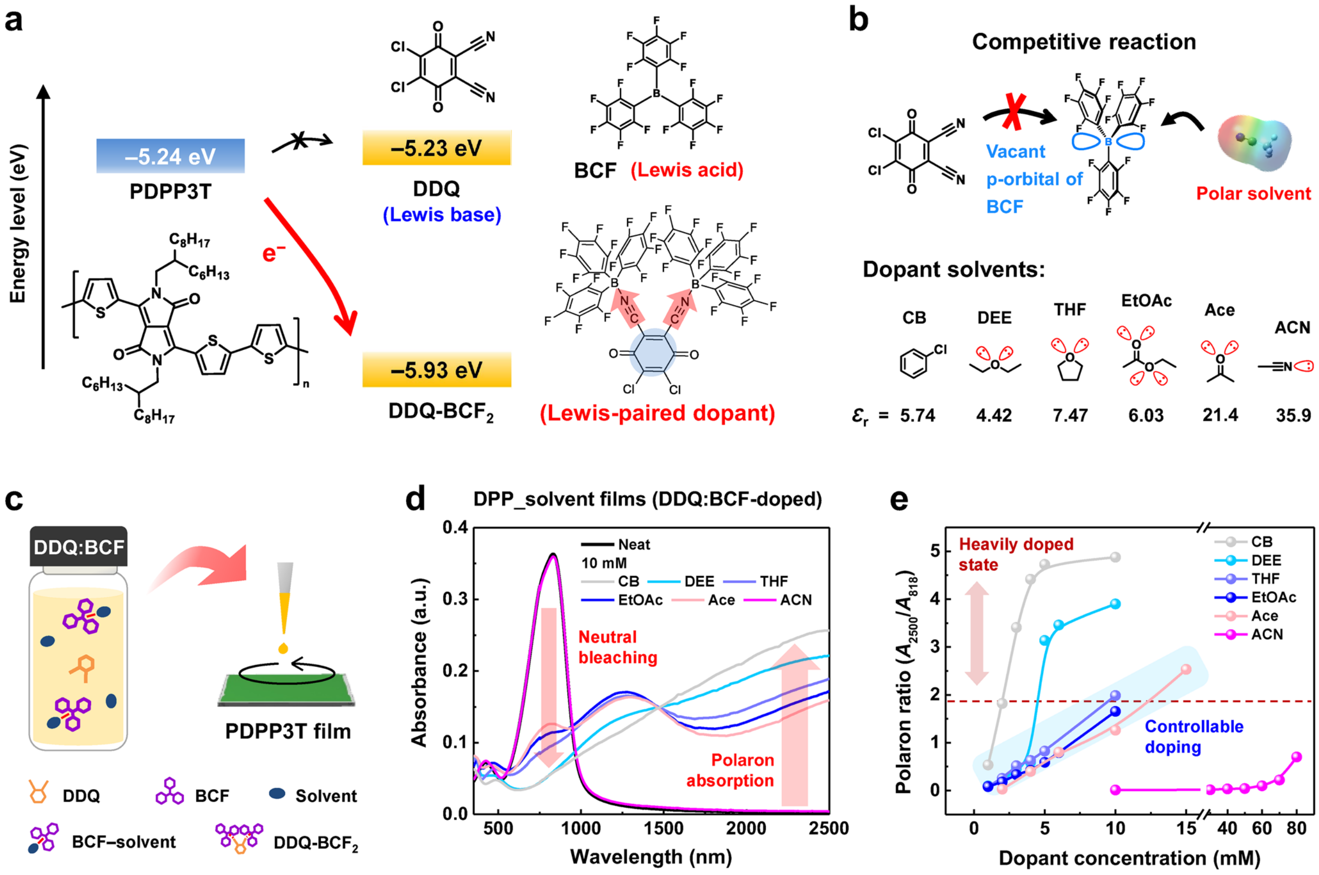

FIGURE 1 | a) Chemical structures and energy levels of PDPP3T, DDQ, BCF, and DDQ:BCF (DDQ-BCF$_2$) illustrating the electron-transfer processes from PDPP3T to dopants. b) Schematic illustrating competitive reaction among DDQ, BCF, and solvent molecule with the chemical structures and ε_r values of tested dopant solvents. c) Schematic illustrating SqP doping of PDPP3T film with DDQ:BCF. d) UV–vis–NIR absorption spectra of neat PDPP3T film and DPP_solvent films (10 mM DDQ:BCF). e) Plots of polaron-to-neutral absorption ratio versus DDQ:BCF concentration for DPP_solvent films. A_{2500} and A_{818} represent the absorbances at 2500 (polaron) and 818 nm (neutral), respectively, in each UV–vis–NIR absorption spectrum.

On doping, charge carriers generated in OSCs (i.e., polarons) create new electronic states within the bandgap. These in-gap states can be directly probed by UV–visible–near infrared (UV–vis–NIR) spectroscopy because polaron formation enhances NIR absorption while diminishing the visible absorption of neutral OSCs [38, 39]. Accordingly, we measured the UV–vis–NIR spectra of the neat PDPP3T film and PDPP3T films doped with DDQ:BCF using the six solvents for SqP (DPP_solvent films) (Figure 1d). These DPP_solvent films were prepared with a uniform neat-film thickness (40 ± 3 nm) and the same dopant concentration (10 mM) to enable a direct comparison of doping efficiency. Notably, no additional thermal annealing step was applied after dopant deposition during the SqP process in this study. The spectrum of the DPP_CB film displayed an almost completely bleached neutral peak around 818 nm and the strongest (bi)polaron peak across 1000–2500 nm, indicating vigorous p-doping of PDPP3T, consistent with our previous work [18]. The extent of neutral peak bleaching and (bi)polaron peak absorption followed the order CB > DEE > THF > EtOAc > Ace > ACN, which showed a rough inverse correlation with the trend in solvent ε_r: DEE (4.42) < CB (5.74) < EtOAc (6.03) < THF (7.47) < Ace (21.4) < ACN (35.9) [40]. These results suggest that more polar solvents hinder the formation of DDQ:BCF more strongly, likely because of the coordination of unpaired electrons to the vacant p-orbital of BCF, thereby reducing doping efficiency.

Next, we varied the dopant concentrations and measured the spectra of the resulting films to examine whether the doping level could be systematically controlled (Figure S3). To this end, we plotted the polaron-to-neutral absorption ratios of the films (A_{2500}/A_{818}) as a function of dopant concentration (Figure 1e), where a consistent, sizable slope indicates doping tunability in the tested range [41, 42]. The polaron ratios of DPP_CB films steeply increased and saturated first (≈4.5 at around 4 mM). Based on a recent study by Murrey et al., the polaron density of the DPP_CB film (2 mM) was estimated to exceed 4×10^{20} cm^{-3}, reaching a heavily doped state even at a low dopant concentration [43]. However, controlling the polaron density at lower doping levels was difficult because this film lost approximately 60%–75% of its initial thickness (Figures S3a and S4) and the loss became more severe at lower dopant concentrations. The DPP_DEE films showed a similar trend in the plot with a slightly larger saturation concentration and lower polaron ratio (≈3 at around 5 mM). In contrast, the DPP_ACN films exhibited extremely low polaron ratios even at considerably higher dopant concentrations with sufficient soaking (90 s) in SqP. Furthermore, the increased absorption in the 350–500 nm range at higher dopant concentrations indicates the presence of residual DDQ and BCF, which may act as impurities (Figure S3g) [44]. The polaron ratios of the DPP_THF, DPP_EtOAc, and DPP_Ace films increased moderately to values between 1.7 and 2.5 across dopant

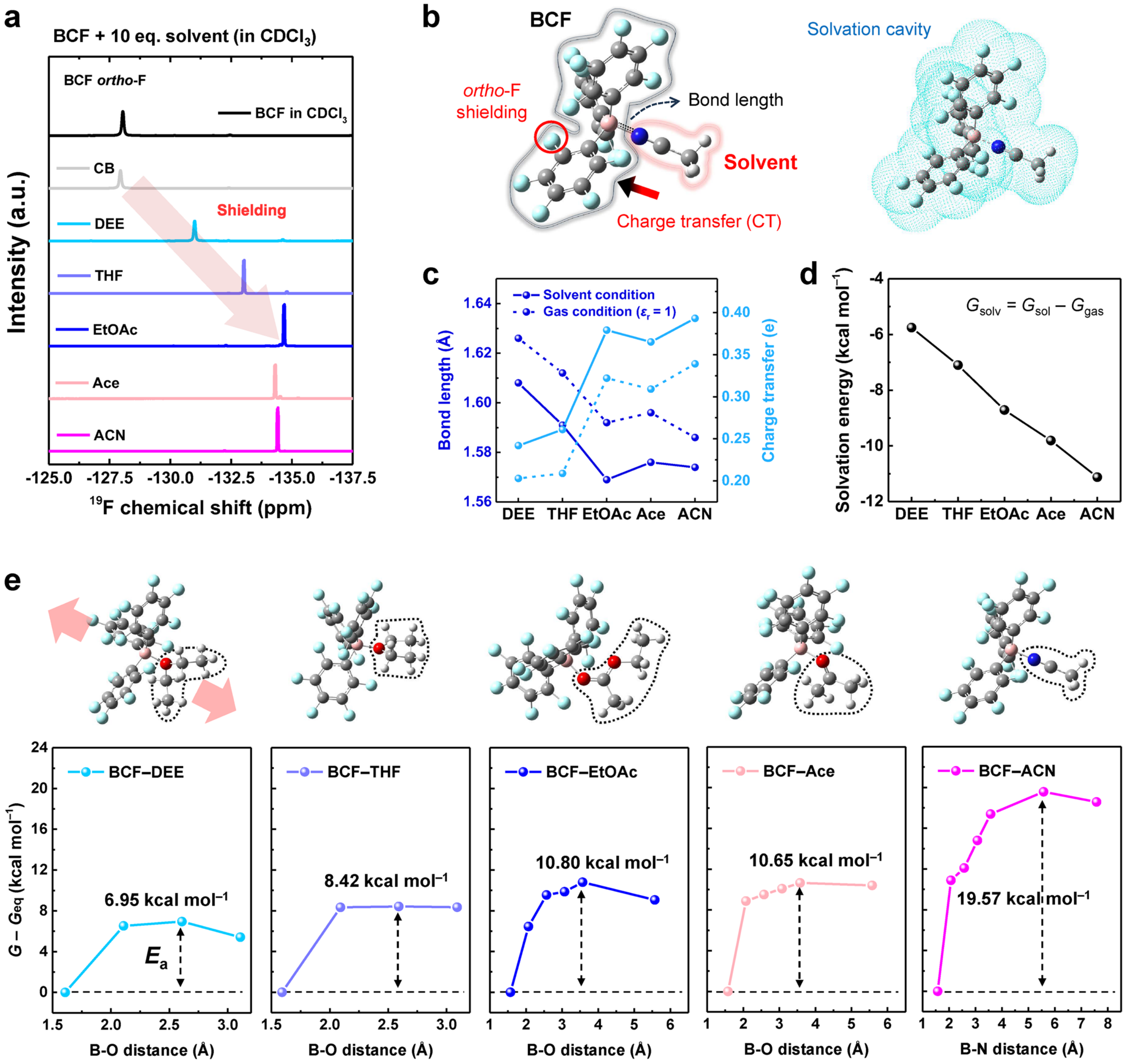

FIGURE 2 | a) ^{19}F NMR spectra of BCF solutions in CDCl$_3$ before and after the addition of various solvents (10 eq. to BCF). b) Optimized structures of BCF–ACN in the gas phase (left) and solvated condition with a solvation cavity (right). The structure on the left displays the *ortho*-F atom position studied in (a), direction of CT, and B-solvent bond. c) Calculated B-solvent bond lengths of BCF–solvent adducts for five different solvents and extent of CT from solvent to BCF in the gas-phase (dashed line) and solvated (solid line) conditions. d) G_{solv} of BCF–solvent adducts for five different solvents. A more negative G_{solv} indicates the greater stability of the BCF–solvent adduct in the solution. e) Optimized structures of BCF–solvent adducts for five different solvents and Gibbs free energy changes of the corresponding adducts with increasing B-solvent bond length, together with E_a values.

concentration ranges of 1–2 to 10–15 mM, exhibiting linear trends with slopes of 0.21, 0.18, and 0.15, respectively. These results confirm that the doping level can be finely tuned within a polaron density range of 10^{19}–10^{21} cm^{-3} by adjusting DDQ:BCF concentrations when using THF, EtOAc, or Ace as the dopant solvents (Figures S5 and S6).

^{19}F nuclear magnetic resonance (NMR) spectroscopy was used to investigate the effect of solvent polarity on the molecular interactions between the BCF and the solvent molecules [45]. Figure 2a shows the ^{19}F NMR spectra of BCF solutions in CDCl$_3$ before and after the addition of each solvent at 10 equivalents (eq.) relative to BCF. All spectra exhibited a single BCF *ortho*-F peak rather than two distinct peaks corresponding to free BCF and BCF–solvent adducts. This observation is attributed to a rapid exchange between the two species (BCF + solvent $\rightleftharpoons$ BCF–solvent), which resulted in a time-averaged signal or full association of solvents to BCF [46]. For the CB-added solution, a single peak appeared at nearly the same position (−127.9 ppm) as that of the neat BCF solution (−128.0 ppm). The peak shifted progressively upfield to −134.7 ppm (EtOAc) with an increase in the solvent ε_r, indicating increased electron donation from the solvent to the BCF and a reduced fraction of free BCF. This upfield shift trend inversely correlates with the doping efficiency trend of the polymer films (CB > DEE > THF > EtOAc), as shown in Figure 1d. However, further increases in ε_r beyond EtOAc did not result in additional upfield shifts (Ace: −134.3 ppm; ACN: −134.4 ppm) even though the doping efficiency with ACN was markedly different from that with Ace and EtOAc. These results imply that the formation of BCF–solvent adducts becomes saturated in all the three cases (EtOAc, Ace, and ACN), and the extents of electron donation are similar. Therefore, other factors must be considered to account for the large discrepancy in the doping efficiency between DPP_ACN and the other films.

Most BCF molecules can exist as BCF–solvent adducts in polar solvent-rich environments, and therefore, the stability of these Lewis adducts play a crucial role in doping efficiency. To investigate the correlation between solvent polarity and BCF–solvent stability, density functional theory (DFT) calculations were conducted to estimate the bonding characteristics and thermodynamic parameters of the Lewis adducts (Figure 2b–d) [35]. The optimized structure revealed that CB did not form any chemical bonds with the boron atom of BCF (Table S1). For the other solvents, the binding free energy (ΔG) became more negative from BCF–DEE (−3.89 kcal mol^{-1}) to BCF–ACN (−9.22 kcal mol^{-1}) as the solvent polarity increased, with a slightly deviating value for BCF–Ace (−5.75 kcal mol^{-1}). This trend indicates that free BCF is thermodynamically favored in less-polar solvents.

Bonding characteristics between the BCF and the solvents provide further insight into the stability of the Lewis adducts (Figure 2b,c) [35]. In both gas-phase and solvated conditions, the B-solvent bond length decreased in the order of DEE > THF > EtOAc ≈ Ace ≈ ACN, whereas the corresponding charge transfer (CT) values showed opposite but similar trends, which increased with polarity. These results indicate that the BCF–solvent adducts become more stable with an increase in solvent polarity, with shorter bond lengths and greater CT values, consistent with the ^{19}F NMR results shown in Figure 2a. Furthermore, we evaluated the solvation energy (G_{solv}) for the Lewis adducts to assess the effect of stabilization by a solvent-induced electric field (Figure 2b,d) [47]. The G_{solv} values became more negative nearly linearly in the order of DEE > THF > EtOAc > Ace > ACN, which closely matched the observed doping efficiency trend. Because the formation of free BCF in SqP can be controlled kinetically, we investigated the dissociation rates of the BCF–solvent adducts by calculating the activation energy (E_a) required to dissociate the Lewis adducts. Figure 2e shows changes in the Gibbs free energy of each BCF–solvent as a function of increasing B-solvent bond length along with the corresponding E_a values and optimized structure schemes. The E_a values increased in the order of DEE < THF < EtOAc ≈ Ace < ACN, showing an inverse correlation with the observed doping efficiency trend. Despite the similar bond lengths and CT values (Figure 2c), the E_a of BCF–ACN was nearly twice as high as those of BCF–EtOAc and BCF–Ace. Because a higher activation energy directly translates into slower dissociation kinetics, BCF–ACN is expected to have a significantly slower dissociation rate than those of the other Lewis adducts.

To study the coordination kinetics of BCF with the solvents, we performed ^{13}C and ^{19}F NMR spectroscopy on the BCF solutions in $CDCl_3$ with varying amounts of EtOAc or ACN (0.1–10 eq. to BCF). We focused on these two representative solvents, which led to a large discrepancy in the doping efficiency for the remaining analyses and measurements. Figure 3a shows the ^{19}F NMR spectra of BCF solutions with the solvent additives, along with equilibrium schemes between the BCF and solvents. The BCF *ortho*-F peak gradually shifted from −127.9 to −134.7 ppm with an increase in the amount of EtOAc. Notably, all *ortho*-F peaks appeared as a single peak positioned between those of free BCF and BCF–EtOAc, indicating a dynamic equilibrium state. In contrast, upon the addition of ACN, the ^{19}F NMR signals appeared only at two distinct peak positions, which corresponded to the free BCF and BCF–ACN. Furthermore, at 0.1 and 0.5 eq. conditions, the two peaks were observed simultaneously, indicating the coexistence of separately stabilized free BCF and BCF–ACN. The ^{13}C NMR spectra exhibited peak shift trends similar to those of the ^{19}F NMR spectra (Figure S7). These results confirmed that the lifetimes of the BCF–EtOAc and BCF–ACN complexes are shorter and longer, respectively, than the NMR timescale, and that BCF–EtOAc exhibits a faster dissociation rate than BCF–ACN, which is consistent with their E_a values (Figure 2e).

We then investigated how the dissociation rate of the BCF–solvent affects the formation kinetics of DDQ:BCF Lewis pairs by measuring the ^{13}C NMR spectra of DDQ and DDQ:BCF solutions with varying amounts of EtOAc or ACN (1–10 eq. relative to DDQ). In the absence of EtOAc and ACN, DDQ exhibited sharp ^{13}C NMR peaks at 140.728 (C1), 169.028 (C2), 124.213 (C3), and 109.564 ppm (C4), which shifted by +0.468 (downfield), −1.772 (upfield), −1.825 (upfield), and −2.925 ppm (upfield), respectively, upon the formation of DDQ:BCF (Figure 3b; Figure S8). The extents of these peak shifts (C1–C4) caused by DDQ:BCF formation progressively decreased with an increase in the amount of solvent additive (Figure 3b,c; Figure S9–S12). These results indicate that even small amounts of solvent additives (10 eq. ≈ 3 vol%) can hinder the formation of DDQ:BCF. However, the C1 peak of DDQ still exhibited a downfield shift of 0.023 ppm (≈14 Hz) upon DDQ:BCF formation in the presence of 10 eq. EtOAc, which is nearly three times larger than the shift observed with 10 eq. ACN (0.008 ppm ≈ 5 Hz) (Figure 3b,c). Comparable trends were observed for C2, C3, and C4, indicating that DDQ:BCF forms more readily in the presence of EtOAc than that of ACN (Figures S9–S12). Collectively, the ^{19}F and ^{13}C NMR results clearly demonstrate that the rapid dissociation of the BCF–solvent adduct is key to facilitating the formation of DDQ:BCF, as illustrated in Figure 3d.

To examine the feasibility of doping-level control using the solvent-mediated Lewis-paired dopants, we evaluated the TE performance of DDQ:BCF-doped PDPP3T films, given that σ and S are highly sensitive to the doping level of semiconductors [48]. Figure 4a presents the plots of σ versus dopant concentration for DPP_EtOAc and DPP_ACN films with a gray dashed line marking the maximum σ of DPP_CB films (Figure S13). The σ of the DPP_EtOAc films initially increased and then decreased with dopant concentration, reaching a maximum σ of 38.5 S cm^{-1} at 6 mM, which exceeded that of DPP_CB films (9.3 S cm^{-1}). In contrast, DPP_ACN films exhibited a significantly lower maximum σ of 2.2 S cm^{-1} and required a tenfold higher dopant concentration (60 mM) to reach their optimal value. The lower optimal dopant concentration of the DPP_EtOAc films strongly supports that the formation of DDQ:BCF occurs more readily in

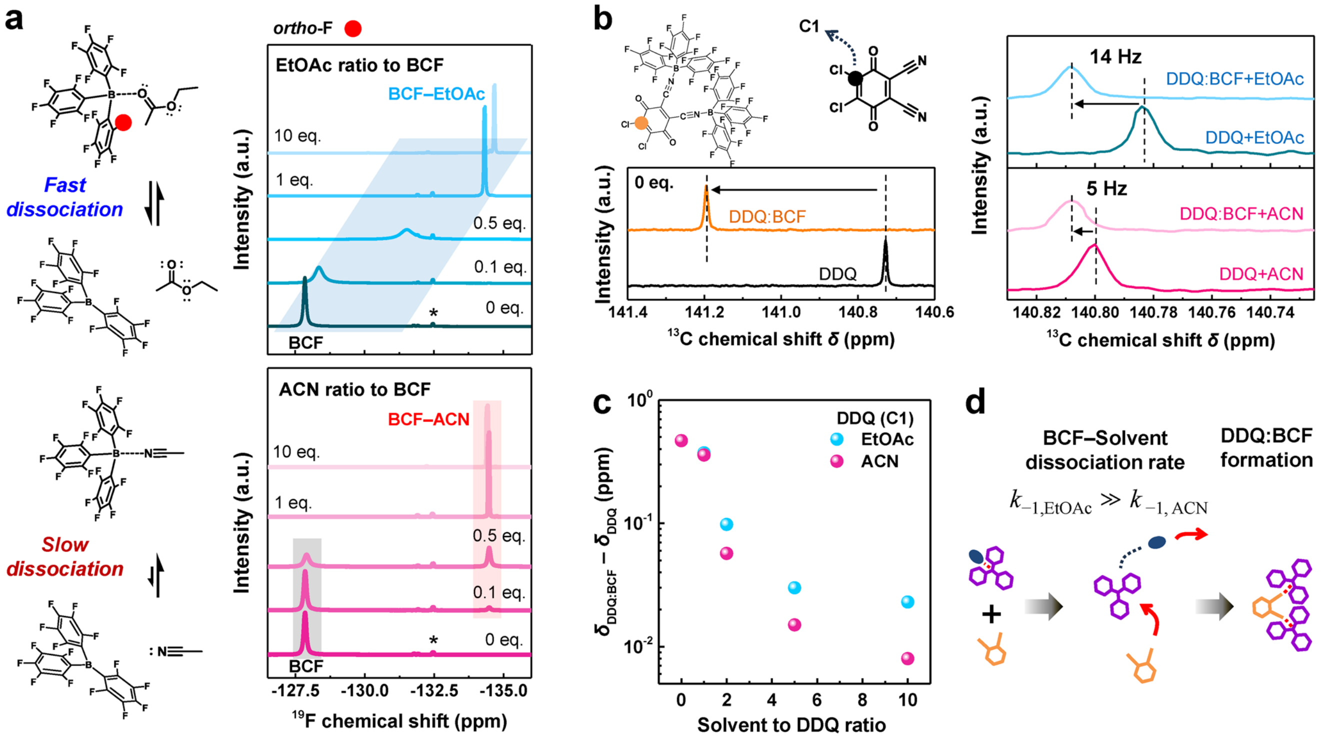

FIGURE 3 | a) ^{19}F NMR spectra of BCF solutions in $CDCl_3$ with varying amounts of EtOAc (top) and ACN (bottom) (0.1–10 eq. to BCF), and schemes of dynamic equilibria between BCF and solvent molecules (BCF + solvent $\rightleftharpoons$ BCF–solvent). Asterisks in the graphs indicate some minor BCF–water adducts caused by trace water in the solvents. b) ^{13}C NMR spectra of DDQ and DDQ:BCF solutions in toluene-d_8 before (left) and after (right) solvent addition (EtOAc or ACN, 10 eq. to DDQ). Solution preparation details are provided in the Experimental Section. The left molecular structures highlight the C1 position of DDQ. c) Chemical shift (C1) differences in the ^{13}C NMR spectra between DDQ and DDQ:BCF as a function of the amount of added solvent. d) Schematic diagram of the mechanism of DDQ:BCF formation in polar solvents highlighting the importance of the dissociation rate of BCF–solvent adducts.

EtOAc than in ACN. Similar behaviors were consistently observed for the DPP_DEE, DPP_THF, and DPP_Ace films (Figure S14). Meanwhile, the S of OSCs can be expressed as [49, 50].

$$S = -\frac{E_T - E_F}{eT} \tag{4}$$

where E_T, E_F, and e represent the transport level, Fermi level, and elementary charge, respectively. As the doping level increases, E_F approaches the HOMO level, and S decreases correspondingly [51]. As shown in Figure 4b, both DPP_EtOAc and DPP_ACN films exhibited decreasing S values with increasing dopant concentration. At comparable S values ($\approx$227 μV K^{-1}), the DPP_EtOAc films (4 mM) exhibited a 15.3-fold higher σ of 33.0 S cm^{-1} than that of the DPP_ACN films (60 mM). Consequently, the DPP_EtOAc films yielded a maximum PF of 170 μW m^{-1} K^{-2}, which is more than an order of magnitude higher than that of the DPP_ACN films (10.9 μW m^{-1} K^{-2}) (Figure 4c).

As noted above, even a small amount of polar solvent (3 vol%) was sufficient to hinder the formation of DDQ:BCF, which suggested that DDQ and BCF may be largely dissociated in the dopant solutions in polar solvents. However, PDPP3T could only be doped with DDQ:BCF and not with the individual components during SqP (Figure S2). Then, the key question is how the doping of PDPP3T proceeds with DDQ:BCF in EtOAc and ACN. We inferred that free BCF can still coordinate with DDQ in polar solvent media because the BCF–solvent adducts exist in dynamic equilibrium at room temperature for solvents with moderate polarity (Figure 3a). This inference is supported by the decreased neutral peak absorption of PDPP3T films immersed in DDQ:BCF solutions in EtOAc or ACN over time, with a decrease occurring more rapidly in EtOAc, especially in the early stage (Figure S15). In addition, suppressed doping was observed even with a small amount of ACN in a mixed solvent system of methyl acetate and ACN (Figure S16). Based on these considerations, we proposed a doping mechanism for the PDPP3T films with DDQ:BCF during SqP (Figure 4d). This interpretation, grounded in the series of equilibria described above (Equations (1)–(3)), is further supported by the quantification of the kinetics of BCF–solvent exchange derived from additional ^{19}F NMR and time-dependent absorbance analyses, as detailed in the Supporting Information (Figures S17–S20). Upon the deposition of the DDQ:BCF solution onto a spinning PDPP3T film, the solvent evaporated, and BCF–EtOAc dissociated to release free BCF, which subsequently coordinated with DDQ to induce the p-doping of the PDPP3T film. Therefore, the faster the BCF–solvent dissociation rate, the more readily DDQ:BCF can be formed, leading to a higher doping efficiency. In contrast, for the dopant solution in ACN, a higher dopant concentration and longer doping time were required to generate free BCF because of the slower BCF–ACN dissociation rate. However, this resulted in significantly more inactive dopants (free DDQ and BCF), which may act as impurities, hindering charge transport in the doped PDPP3T films.

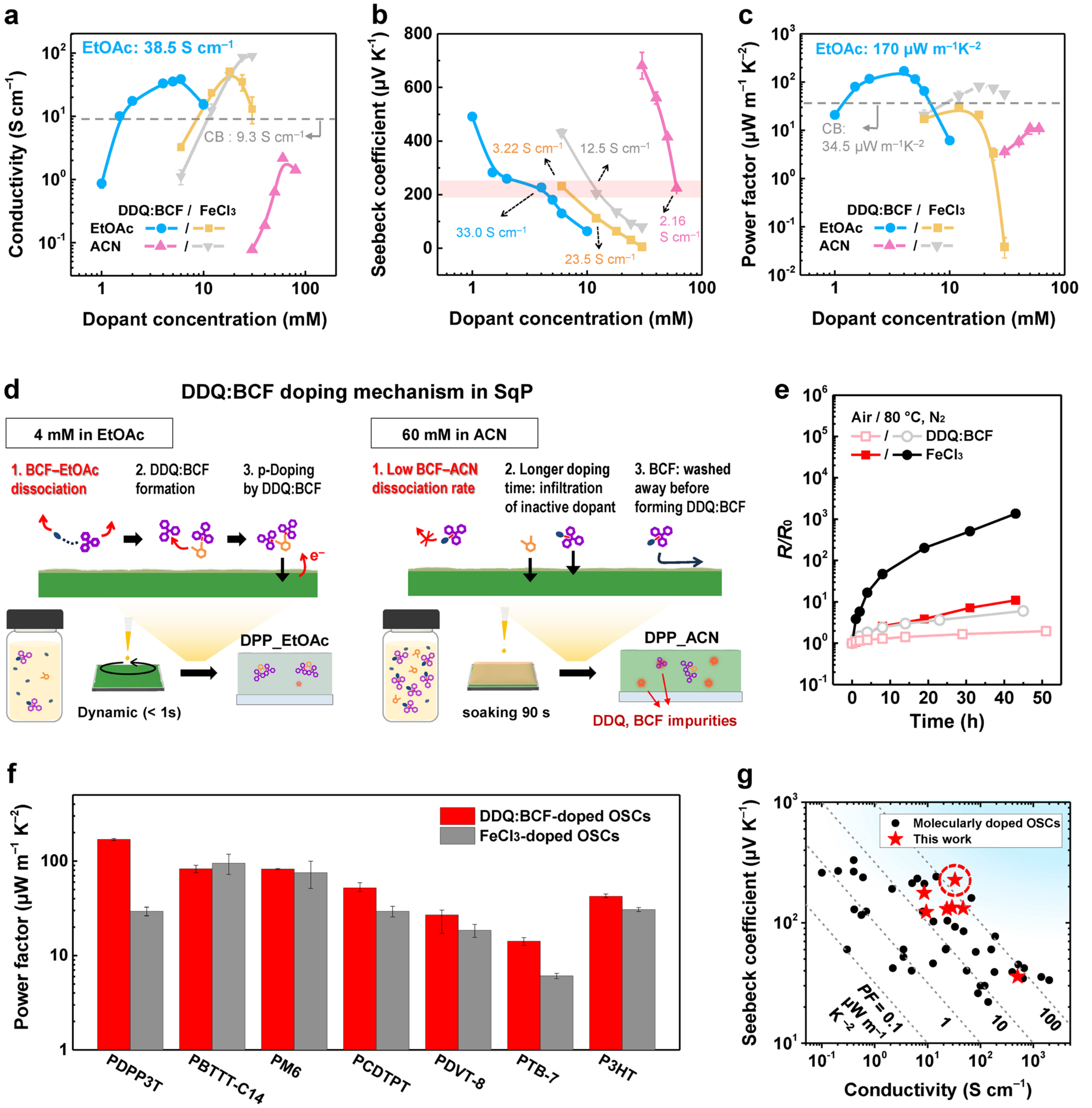

FIGURE 4 | TE performances of DPP_EtOAc, DPP_ACN, and FeCl$_3$-doped PDPP3T films as functions of dopant concentration: a) σ, b) S, and c) PF, with standard error obtained from three to six independently measured devices. Gray dashed lines represent the maximum values of DDQ:BCF-doped PDPP3T films processed with CB. d) Schematic diagram of the DDQ:BCF doping mechanisms during SqP with EtOAc (left) or ACN (right). e) Resistance changes over time for PDPP3T films doped with DDQ:BCF or FeCl$_3$ under different conditions (in air or at 80°C in N$_2$). f) PF values of various OSC films doped with DDQ:BCF or FeCl$_3$ at optimal conditions, with standard error obtained from three to six independently measured devices. g) S versus σ plots for various OSC films doped with organic dopants reported in the literature, including this study [24, 52–60]. Each dashed line indicates the same PF value.

FeCl$_3$ is one of the most widely used p-dopants because of its high oxidation strength [61]; therefore, the TE performances of FeCl$_3$-doped PDPP3T films (EtOAc and ACN as the dopant solvent) were evaluated for comparison (Figure 4a–c; Figure S21). As shown in Figure 4a, the maximum σ of the FeCl$_3$-doped PDPP3T films (89.4 S cm^{-1}) was higher than that of the DPP_EtOAc films. Importantly, however, the DPP_EtOAc films exhibited more than two times higher maximum PF than that of the FeCl$_3$-doped PDPP3T films (82.7 μW m^{-1} K^{-2}) (Figure 4c), reflecting a more favorable balance between σ and S (Figure 4b). To further analyze the transport characteristics, we also plotted the σ and S values of the DDQ:BCF- and FeCl$_3$-doped films and fitted the data using the Kang–Snyder model (Figure S22) [62]. From the fitting, the highest transport coefficient (σ_{E0}) of 50 S cm^{-1} was extracted for the DPP_EtOAc films, compared with 30 and 10 S cm^{-1} for the $FeCl_3$-doped films processed with ACN and EtOAc, respectively. These results indicate more efficient charge transport in the DDQ:BCF-doped system. We think that larger DDQ:BCF anions may exert weaker Coulombic interactions with the generated polarons than the smaller $FeCl_3$ anions, enhancing the contribution of the polarons to electrical conduction [28, 63].

We compared the stability of the DPP_EtOAc (4 mM) and $FeCl_3$-doped PDPP3T (10 mM) films because the larger size of DDQ:BCF can contribute to a higher doping stability than $FeCl_3$ doping. The dopant concentrations were selected to roughly match their doping levels because doping stability can vary based on the degree of doping [64]. Figure 4e shows the sheet resistance changes (R/R_0) of these samples over time in air at room temperature or in an N_2 atmosphere at 80°C. Under both conditions, the DPP_EtOAc films exhibited superior stability compared to the $FeCl_3$-doped PDPP3T films. Similar trends were observed in their UV–vis–NIR spectra (Figure S23). Although the stability of the DPP_EtOAc films was relatively lower than that of the PDPP3T films doped with a bulkier Lewis-paired dopant in our previous study [18], DDQ:BCF doping clearly outperformed $FeCl_3$ doping in terms of both TE performance and doping stability.

We also tested six different OSCs with SqP using DDQ:BCF solutions in EtOAc to demonstrate the broad applicability of this Lewis pairing doping strategy. All DDQ:BCF-doped OSCs showed finely controlled doping levels as observed by UV–vis–NIR spectroscopy (Figures S24–S29), which enabled the optimization of their TE performances, as summarized in Figure 4f and Table S2. Remarkably, the optimized *PF* values of the DDQ:BCF-doped OSC films exceeded those of their $FeCl_3$-doped counterparts in most cases, highlighting the effectiveness of the Lewis-paired doping system (Figure 4f; Figures S30–S35). Furthermore, superior *PF* and *S* values were simultaneously achieved for the other OSCs, similar to the case of PDPP3T (Figure 4f,g). Interestingly, DDQ:BCF doping was also effective for PCDTPT, which contains Lewis basic pyridine moieties, yielding high σ and *PF* of 64.6 S cm^{-1} and 51.9 μW m^{-1} K^{-2}, respectively (Figure S24). Such Lewis basic polymers are known to form Lewis complexes with BCF, and therefore, doping with BCF alone resulted in poor electrical properties ($\sigma < 1$ S cm^{-1}) [52, 53]. These results indicate that the coordination between BCF and DDQ is more favorable than that between BCF and the pyridine moiety, suggesting that the Lewis-paired dopants can also be applied to Lewis-basic OSCs, which largely include high-performance donor–acceptor type conjugated polymers with deep HOMO levels.

2D grazing incident X-ray diffraction (2D-GIXD) measurements were performed to examine the effect of DDQ:BCF doping on the molecular ordering of the DPP_EtOAc and DPP_ACN films (Figure 5). OSC films undergo structural rearrangement upon solvent exposure, depending on solvent polarity [65]. Therefore, we confirmed that the edge-on molecular orientation of the neat PDPP3T film was well preserved after exposure to the tested dopant solvents, except for CB, which almost completely destroyed the molecular ordering (Figure S36). Furthermore, PDPP3T films exposed to EtOAc and ACN exhibited nearly identical crystallographic parameters (Table S3), indicating that the difference in TE performance between the DPP_EtOAc and DPP_ACN films may not be attributable to solvent exposure effects. Instead, we attributed this difference to their distinct doping mechanisms, as shown in Figure 4d. Figure 5a shows the 2D-GIXD patterns of the neat PDPP3T, DPP_EtOAc (4 mM), and DPP_ACN (60 mM) films (additional patterns at other dopant concentrations are shown in Figures S37 and S38). All 2D-GIXD patterns show a clear edge-on molecular orientation of PDPP3T, which indicates the preservation of molecular ordering after doping, unlike in the case of the DPP_CB films (Figure S39).

Figure 5b presents the corresponding out-of-plane and in-plane line-cut profiles of 2D-GIXD patterns from which lamellar *d*-spacing and π–π stacking distance values were extracted (Tables S4 and S5). The molecular ordering of doped polymers can be altered either by the infiltration of dopants into ordered structures or by chain rearrangement to stabilize the generated polarons [66, 67]. Therefore, to compare the crystallographic parameters at similar doping levels, the lamellar *d*-spacing and π–π stacking distances of the DPP_EtOAc and DPP_ACN films were plotted as a function of the polaron ratio (A_{2500}/A_{818}) (Figure 5c), which was defined in Figure 1e based on the UV–vis–NIR spectra (Figure S3). The lamellar *d*-spacing of both the DPP_EtOAc and DPP_ACN films progressively increased with the polaron ratio, from 17.8 Å (Neat) to 19.9 Å (EtOAc, 6 mM dopant) and 18.53 Å (ACN, 80 mM dopant). The DPP_EtOAc films exhibited larger lamellar *d*-spacing values than those of the DPP_ACN films at similar doping levels despite considerably lower dopant concentrations (Figure 5c). These results indicated that more dopant molecules infiltrated into the lamellar region of DPP_EtOAc, whereas they were mainly positioned in the amorphous region of DPP_ACN [23, 68]. In contrast, the π–π stacking distances of the DPP_EtOAc films decreased from 3.99 Å (Neat) to 3.89 Å (6 mM), suggesting the enhanced backbone planarity of PDPP3T upon doping [26]. Meanwhile, those of the DPP_ACN films decreased only marginally from 3.99 Å (Neat) to 3.97 Å (80 mM). The more pronounced reduction in the π–π stacking distance in the DPP_EtOAc films likely contributed to their higher TE performance by facilitating charge transport compared to the DPP_ACN films. Additional 2D-GIXD analyses were performed on DPP_DEE, DPP_THF, and DPP_Ace films (Figure S40). While the DPP_THF film exhibited slightly disrupted molecular ordering accompanied by relatively lower TE performance (Figure S14), the overall molecular ordering was largely preserved across the different solvent systems.

To better understand the origin of the superior TE performance of the DPP_EtOAc films, we performed Raman and Fourier transform infrared (FTIR) measurements. Raman spectroscopy provides information on the chain conformation and backbone planarity of OSCs, which are directly related to their charge transport abilities [69, 70]. Considering the neutral PDPP3T absorption (Figure 1d), an incident laser wavelength of 785 nm was used. As shown in Figure 6a, the neat PDPP3T film exhibited three strong Raman bands at 1368, 1422, and 1508 cm^{-1}, consistent with a previous report [69]. Thereafter, we measured the Raman spectra of the DPP_EtOAc and DPP_ACN films at various dopant concentrations (Figure S41). The two films showed different trends with increasing dopant concentration, particularly in the 1422 cm^{-1} band, which corresponded to the symmetric stretching of C–C bonds in the conjugated backbone (Figure 6a inset). The DPP_EtOAc films showed a gradual red-shift to 1417 cm^{-1} (6 mM), whereas the DPP_ACN films exhibited

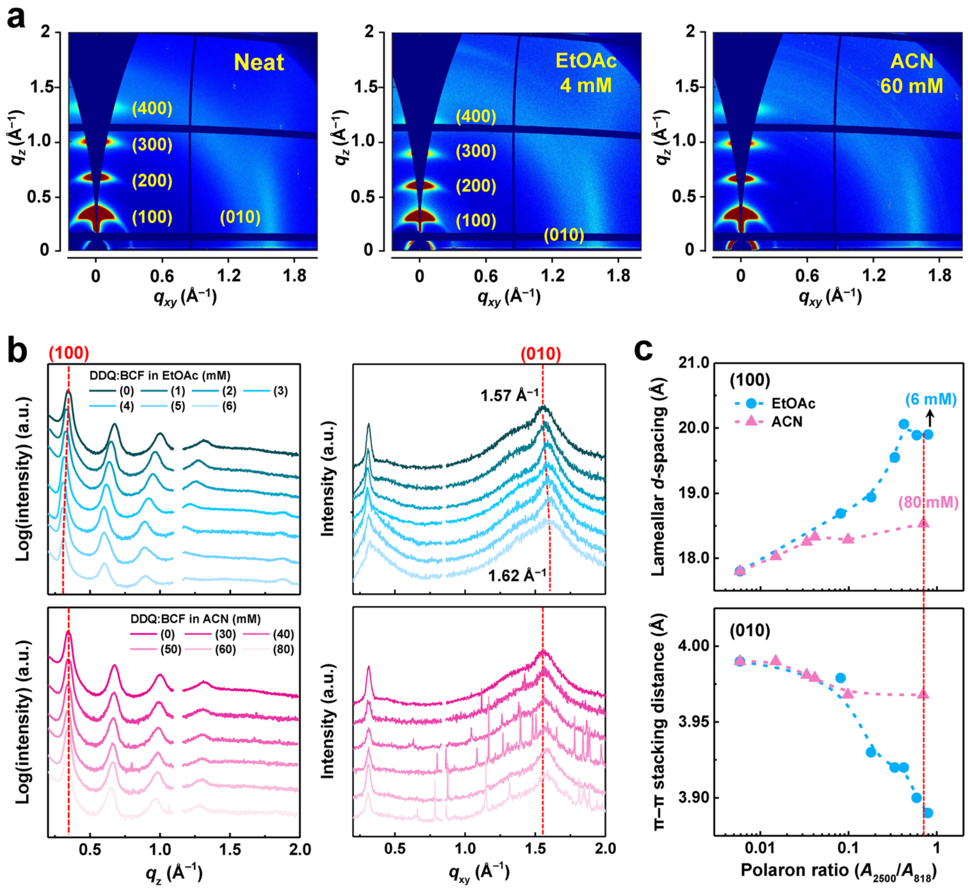

FIGURE 5 | a) 2D-GIXD patterns of neat PDPP3T, DPP_EtOAc (4 mM), and DPP_ACN (60 mM) films. b) Line-cut profiles from the 2D-GIXD patterns of DPP_EtOAc (top) and DPP_ACN (bottom) films at various dopant concentrations along the out-of-plane (left) and in-plane (right) directions. c) Lamellar *d*-spacing (top) and *π*–*π* stacking distances (bottom) as functions of polaron ratio.

negligible shifts (Figure 6a; Figure S41). These results indicate that the PDPP3T in DPP_EtOAc films has more planar chain conformation, as deduced from the tighter *π*–*π* stacking distances (Figure 5c).

Figure 6b shows the FTIR spectra of the DPP_EtOAc (4 mM) and DPP_ACN (60 mM) films (additional spectra at other dopant concentrations are shown in Figure S42). The DPP_EtOAc films displayed a mid-IR polaron absorption band centered at ≈2500 cm^{-1}, which was significantly lower than that of the DPP_ACN films (≈3000 cm^{-1}), indicating longer polaron delocalization lengths in PDPP3T for the DPP_EtOAc films [28]. This trend was evident even for the DPP_EtOAc film at very low dopant concentrations (1 mM) compared to the DPP_ACN films at 60 and 80 mM, which had similar or higher doping levels. In general, the polaron delocalization length in doped OSC films is influenced by energetic and structural disorder [71, 72]. Therefore, we performed additional experiments, including DFT calculations, to examine changes in the CN bands of the FTIR spectra (2150–2275 cm^{-1}) upon DDQ:BCF doping (Figures S43–S45). These studies revealed that the DPP_ACN films contained neutral DDQ:BCF, which can act as impurities, and a charge-transfer complex (CTC) between DDQ and the PDPP3T backbone [73–75], which can hinder the *π*–*π* stacking of PDPP3T and localize the polarons (see the Supporting Information for details).

Then, we performed X-ray photoelectron spectroscopy (XPS) depth profiling to compare the relative compositions of DDQ and BCF in the DPP_EtOAc and DDP_ACN films (Figure S46). Given the unique atoms of Cl (DDQ), F (BCF), and S (thiophene moiety of PDPP3T), the relative contents of DDQ and BCF were estimated by calculating the Cl/S and F/S ratios, respectively. The DPP_ACN film was prepared under modified SqP conditions with a higher dopant concentration (100 mM) but a lower spinning speed (1000 rpm) to minimize the dopant residue caused by centrifugal force (see the Experimental Section for details). This resulted in a similar doping level to that of the normally prepared DPP_ACN film at 70 mM (Figure S47). Despite the considerably higher dopant concentration and longer soaking time, the DPP_ACN film (100 mM) exhibited markedly lower relative contents of DDQ and BCF than those of the DPP_EtOAc film (4 mM) (Figure 6c). Notably, the DPP_EtOAc film (4 mM) exhibited a relative BCF ratio to DDQ ($N_{\mathrm{BCF}}/N_{\mathrm{DDQ}}$) of 1.85, closely matching the stoichiometry of DDQ-BCF$_2$. In contrast, the DPP_ACN film (100 mM) showed a smaller $N_{\mathrm{BCF}}/N_{\mathrm{DDQ}}$ ratio of 0.77, implying that DDQ-BCF$_1$ was the dominant dopant species. Furthermore, we inferred that the BCF–ACN adducts were swept out during SqP, whereas free DDQ remained in the film because of the slow dissociation rate of BCF–ACN. This residual DDQ could penetrate into the *π*–*π* stacks of PDPP3T and form a CTC with the DPP unit, which disrupted molecular packing and localizing polarons (Figure 6d) [73–75], ultimately

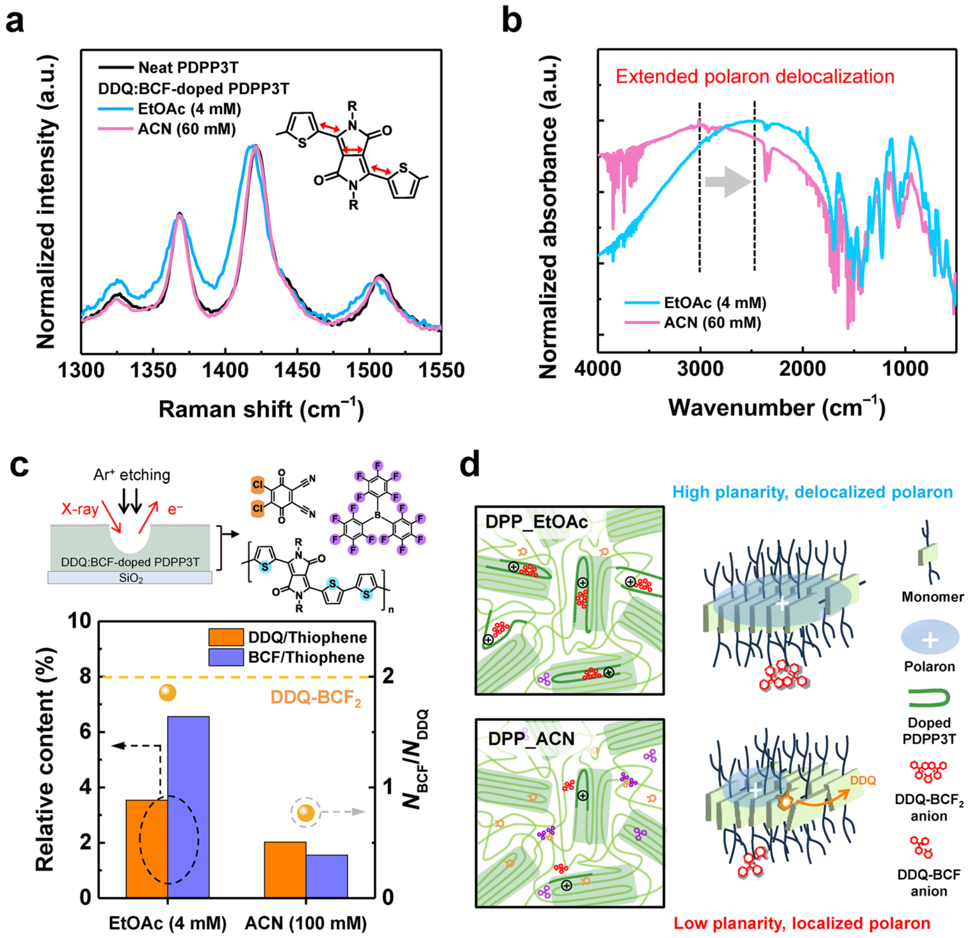

FIGURE 6 | a) Raman spectra of neat PDPP3T, DPP_EtOAc (4 mM), and DPP_ACN (60 mM) films. Inset shows the symmetric stretch of C–C bonds in the conjugated backbone at 1422 cm^{-1}. b) FTIR spectra of DPP_EtOAc (4 mM) and DPP_ACN (60 mM) films. c) XPS-derived relative contents of DDQ and BCF with respect to the thiophene moiety of PDPP3T, together with $N_{\mathrm{BCF}}/N_{\mathrm{DDQ}}$ values of DPP_EtOAc (4 mM) and DPP_ACN (100 mM) films. Yellow dashed line indicates the stoichiometric ratio of DDQ-BCF$_2$. Top schematics illustrate the XPS depth profiling process and molecular structures with highlighted key atoms. d) Schematics of differences in molecular packing structure, backbone planarity, and polaron localization of PDPP3T chains in DPP_EtOAc and DPP_ACN films.

degrading TE performance. On the other hand, higher doping levels and more efficient polaron generation could be achieved for the DPP_EtOAc films at lower dopant concentrations because DDQ-BCF$_2$ is the dominant form, which is expected to possess a stronger oxidizing ability than that of DDQ-BCF$_1$. This high oxidizing strength can even induce mild p-doping in an n-type OSC (N2200) (Figure S45), whose HOMO level was estimated to be −5.92 eV in our previous study [18]. Consequently, DPP_EtOAc films exhibited superior TE performance, which can be attributed to their more planar backbone conformation, longer polaron delocalization lengths, and tighter π–π stacking distances.

3 | Conclusion

We demonstrated a versatile doping strategy via the solvent-mediated reactivity control of the Lewis-paired dopant DDQ:BCF, which enabled the tunable, efficient, and stable doping of diverse OSCs. Spectroscopic analyses supported by DFT calculations revealed that the dissociation rate of BCF–solvent adducts, which strongly depends on solvent polarity, is a key factor for regulating the formation of DDQ:BCF. The DDQ:BCF formed in nonpolar solvents resulted in limited doping-level control and disrupted the ordered structures of the OSC films. Coordination between the BCF and solvent molecules dominated in highly polar solvents, suppressing DDQ:BCF formation and lowering doping efficiency. However, in solvents with optimal polarity, BCF and solvent molecules exist in dynamic equilibrium, enabling DDQ to pair with free BCF upon solvent evaporation during SqP. Consequently, processing with EtOAc enabled the precise doping-level control of various OSCs with high doping efficiency, from simple polythiophene to liquid-crystalline and donor–acceptor type polymers with deep HOMO levels. Consequently, the TE properties of the tested OSCs could be optimized at low dopant concentrations, simultaneously achieving a high S (227 μV K^{-1}) and PF (170 μW m^{-1} K^{-2}). Raman, FTIR, and 2D-GIXD studies showed that OSCs doped with DDQ:BCF using EtOAc exhibited more planar backbones, tighter π–π stacking distances, and longer polaron delocalization lengths. In addition, DDQ:BCF doping outperformed $FeCl_3$ doping in TE performance, as well as in stability under ambient and thermal stress conditions. Overall, our results highlighted the effectiveness of Lewis-paired dopants by establishing a solvent-mediated doping mechanism. We believe that this strategy provides a practical route to overcome the persistent challenges in OSC doping and will be broadly applicable to various (opto)electronic and energy-conversion devices.

4 | Experimental Section

4.1 | Materials

PDPP3T (M_w = 66,759 g mol^{-1}, PDI = 2.12) was purchased from Ossila. PCDTPT (M_w = 65,000 g mol^{-1}, PDI = 2.0), P3HT (M_w = 78,000 g mol^{-1}, PDI < 2.2), PTB7 (M_w = 80,000–120,000 g mol^{-1}, PDI = 2.0–3.0), and N2200 (M_w = 50,000–100,000 g mol^{-1}; PDI = 2.0–3.0) were purchased from 1-Material. PQT-12 (M_w = 16,000 g mol^{-1}, PDI = 2.0) was purchased from American Dye Source. PDVT-8 (M_w > 20,000 g mol^{-1}) was purchased from Lumtec. PBTTT-C14 (M_w = 52,700 g mol^{-1}, PDI = 2.14) was synthesized and purified as described previously [76]. PM6 (M_w = 80,000–200,000 g mol^{-1}; PDI = 2.0–4.0), DDQ (98%), chloroform (anhydrous, 99%), $FeCl_3$ (97%), CB (anhydrous, 99.8%), DEE (anhydrous, 99%), THF (anhydrous, 99.9%), EtOAc (anhydrous, 99.8%), Ace (HPLC grade, ≥ 99.9%), ACN (anhydrous, 99.8%), *o*-1,2-dichlorobenzene (DCB; anhydrous, 99%), $CDCl_3$ (anhydrous, ≥ 99.8 atom% D), and toluene-d_8 (99.6 atom% D) were purchased from Sigma-Aldrich. BCF (97%) was purchased from Tokyo Chemical Industry. All solvents were dehydrated with molecular sieves (Sigma-Aldrich, 3 Å pore size) before use, while the other chemicals were used as received without further purification, except PBTTT-C14.

4.2 | Sample Preparation

Soda-lime glass substrates (2 cm × 2 cm) were cleaned by bath sonication in deionized water with a detergent, followed by successive sonication in Ace and ethanol for 20 min. The cleaned substrates were UV–ozone treated for 20 min prior to OSC coating. The OSCs were dissolved in DCB (10 mg mL^{-1}) on a 100°C hot plate, and then slowly cooled to 25°C. The OSC solutions were spin-coated at 1000 rpm for 60 s, followed by thermal annealing on a 250°C hot plate for 20 min. For PM6, the polymer was dissolved in CB (5 mg mL^{-1}) and spin-coated at 2000 rpm for 60 s, while the annealing condition remained identical (250°C). DDQ:BCF dopant solutions in six different solvents at varying concentrations were prepared by separately dissolving DDQ and BCF in each solvent, mixing them at a 1:2 molar ratio, and diluting with the same solvent to yield the specified concentrations. For SqP doping, the prepared DDQ:BCF solutions were poured onto the OSC films while spinning at 4000 rpm for 20 s. The volume of the dopant solutions for the SqP was 200 µL, whereas those for CB and ACN were 15 µL and 400 µL, respectively. A 90 s soaking process was necessary prior to spinning the dopant solutions in ACN. The DPP_ACN films for XPS depth profiling were fabricated using different SqP conditions to minimize dopant residues on the films (dopant concentration: 100 mM, soaking time: 6 min, and spinning speed: 1000 rpm). The thermal dedoping of DPP_CB films was performed on a 200°C hot plate for 2–40 s. $FeCl_3$ solutions at specific concentrations were prepared in EtOAc or ACN and subsequently poured (200 µL) onto the OSC films during spinning at 4000 rpm for 20 s to fabricate $FeCl_3$-doped PDPP3T films. All fabrications were performed in an N_2-filled glove box, except for substrate preparation.

4.3 | TE Measurements

Sheet resistances were measured using a four-point probe (each tip was 1 mm apart) connected to a Keithley 2400 source meter. Film thicknesses were measured using a surface profiler (Alpha Step IQ, KLA Tencor). Subsequently, the σ of each OSC film was calculated from the measured sheet resistance and thickness values. The S values of the OSC films were measured using a home-built setup, which was also used in previous studies [25, 41, 42, 52, 53]. Two Peltier devices induced temperature differences, each of which was operated using a Keithley 2400 source meter. The thermovoltages and temperatures were measured using a Keithley 2182A nanovoltmeter and Keithley 2700 multimeter, respectively. The thermovoltages were measured across five different temperature differences (<2 K; median value of 300 K), and S was extracted from a linear plot of the thermovoltage versus temperature difference (Figure S48). All measurements were performed in an N_2-filled glove box, except the thickness measurement and air stability test, which were performed in air (relative humidity: 65.1% ± 10.0%, temperature: 24.0°C ± 3.3°C).

4.4 | Material Characterization

^{13}C and ^{19}F NMR spectra were acquired using a 600 MHz NMR spectrometer (VNMRS, Varian). For the NMR sampling of the BCF solutions in EtOAc or ACN, BCF was dissolved in $CDCl_3$ (30 mg mL^{-1}), and each solvent was added to the BCF solution (0.1–10 eq. to BCF). For the DDQ solutions, DDQ was dissolved in toluene-d_8 (10 mg mL^{-1}), and each solvent (1–10 eq. to DDQ) was added to the DDQ solution. For the DDQ:BCF solutions, DDQ (10 mg mL^{-1}) and BCF (100 mg mL^{-1}) were dissolved separately in toluene-d_8. Subsequently, each solvent (1–10 eq. to DDQ) was added to the BCF solution and then mixed with the DDQ solution. ^{13}C NMR spectra of the DDQ and DDQ:BCF solutions were recorded at an identical solvent composition because the aromatic ring solvent (toluene-d_8) can also induce a ^{13}C chemical shift [77, 78]; e.g., for 10 eq. EtOAc, DDQ:BCF in toluene-d_8:EtOAc (97:3, v/v) was compared with DDQ in toluene-d_8:EtOAc (97:3, v/v). UV–vis–NIR absorption and Raman spectra were acquired using a spectrophotometer (V670, JASCO) and Raman spectrometer (DXR3xi, Thermo Fisher Scientific), respectively. FTIR spectra were recorded using an FTIR spectrometer (FT/IR-8X, JASCO) in the transmittance mode and KBr plates as substrates. XPS depth profiling was performed using an X-ray photoelectron spectrometer (K-Alpha plus, Thermo Fisher Scientific) with an Al K_α (1486.6 eV) X-ray source (operating voltage and current: 12 keV and 6 mA, respectively) and Ar^+ sputter-etching (1 keV). 2D-GIXD measurements were conducted using a high-resolution synchrotron X-ray beam source (beam energy = 10.35 keV) with a fixed grazing incidence angle (≈0.16°) at the 3C beamline of the Pohang Accelerator Laboratory, Pohang, Korea. Heavily doped Si wafers covered with SiO_2 (100 nm) were used as substrates for the XPS and 2D-GIXD experiments.

4.5 | Computational Method

DFT calculations were performed using the PBE0-D3 functional and 6-311G(d,p) basis set implemented in the Gaussian 16 W software package. The conditions of the following solvents were set using the conductor-like polarizable continuum model: DEE ($\varepsilon = 4.24$), THF ($\varepsilon = 7.43$), EtOAc ($\varepsilon = 5.99$), Ace ($\varepsilon = 20.5$), and ACN ($\varepsilon = 35.7$). EtOAc was typed as ethylethanoate in the program, and ε represents the dielectric constant used for the calculations [55]. ΔG was obtained as $\Delta G = G_{\mathrm{BCF-S}} - G_{\mathrm{BCF}} - G_{\mathrm{S}}$, where $G_{\mathrm{BCF-S}}$, G_{BCF}, and G_{S} represent the Gibbs free energies of the optimized structures for the BCF–solvent adduct, BCF, and solvent molecule, respectively. G_{solv} was obtained as $G_{\mathrm{solv}} = G_{\mathrm{sol}} - G_{\mathrm{gas}}$, where G_{sol} represents the Gibbs free energy of the optimized BCF–solvent under solvated conditions and G_{gas} represents the Gibbs free energy calculated for the same geometry in the gas phase.

Acknowledgements

This research was supported by the Nano & Material Technology Development Program through the National Research Foundation of Korea (NRF) funded by Ministry of Science and ICT (RS-2024-00402972). This work was also supported by an NRF grant funded by the Korean Government (MSIT) (RS-2025-00556330) and by the Basic Research Laboratory program of the NRF (RS-2025-00512834).

Conflicts of Interest

The authors declare no competing interests.

Data Availability Statement

All data that support the findings of this study are included in the main article and/or the Supporting Information. Additional data are available from the corresponding author upon reasonable request.

References

1. A. D. Scaccabarozzi, A. Basu, F. Aniés, et al., "Doping Approaches for Organic Semiconductors," *Chemical Reviews* 122 (2022): 4420–4492, https://doi.org/10.1021/acs.chemrev.1c00581.

2. W. Zhao, J. Ding, Y. Zou, C. A. Di, and D. Zhu, "Chemical Doping of Organic Semiconductors for Thermoelectric Applications," *Chemical Society Reviews* 49 (2020): 7210–7228, https://doi.org/10.1039/D0CS00204F.

3. I. E. Jacobs and A. J. Moulé, "Controlling Molecular Doping in Organic Semiconductors," *Advanced Materials* 29 (2017): 1703063, https://doi.org/10.1002/adma.201703063.

4. Y. Xu, H. Sun, A. Liu, et al., "Doping: a Key Enabler for Organic Transistors," *Advanced Materials* 30 (2018): 1801830, https://doi.org/10.1002/adma.201801830.

5. K. Walzer, B. Maennig, M. Pfeiffer, and K. Leo, "Highly Efficient Organic Devices Based on Electrically Doped Transport Layers," *Chemical Reviews* 107 (2007): 1233–1271, https://doi.org/10.1021/cr050156n.

6. C. G. Tang, M. C. Y. Ang, K.-K. Choo, et al., "Doped Polymer Semiconductors with Ultrahigh and Ultralow Work Functions for Ohmic Contacts," *Nature* 539 (2016): 536–540, https://doi.org/10.1038/nature20133.

7. V. A. Kolesov, C. Fuentes-Hernandez, W.-F. Chou, et al., "Solution-Based Electrical Doping of Semiconducting Polymer Films over a Limited Depth," *Nature Materials* 16 (2017): 474–480, https://doi.org/10.1038/nmat4818.

8. B. Russ, A. Glaudell, J. J. Urban, M. L. Chabinyc, and R. A. Segalman, "Organic Thermoelectric Materials for Energy Harvesting and Temperature Control," *Nature Reviews Materials* 1 (2016): 16050, https://doi.org/10.1038/natrevmats.2016.50.

9. R. Kroon, D. A. Mengistie, D. Kiefer, et al., "Thermoelectric Plastics: From Design to Synthesis, Processing and Structure–property Relationships," *Chemical Society Reviews* 45 (2016): 6147–6164, https://doi.org/10.1039/C6CS00149A.

10. G. J. Snyder and E. S. Toberer, "Complex Thermoelectric Materials," *Nature Materials* 7 (2008): 105–114, https://doi.org/10.1038/nmat2090.

11. Y. Karpov, T. Erdmann, I. Raguzin, et al., "High Conductivity in Molecularly p-Doped Diketopyrrolopyrrole-Based Polymer: the Impact of a High Dopant Strength and Good Structural Order," *Advanced Materials* 28 (2016): 6003–6010, https://doi.org/10.1002/adma.201506295.

12. W.-H. Park, D.-P. Park, and S. S. Kim, "Highly Efficient Tandem PHOLEDs with Lithium-Doped BPhen/NDP-9-Doped TAPC as a Charge Generation Layer," *Journal of Information Display* 23 (2022): 45–52, https://doi.org/10.1080/15980316.2021.1947403.

13. S.-A. Chen, J.-M. Ni, and M.-Y. Hua, "Thermal Undoping Behavior of $FeCl_3$-Doped Poly(3-octylthiophene)," *Journal of Polymer Research* 4 (1997): 261–265, https://doi.org/10.1007/s10965-006-0032-0.

14. O. Zapata-Arteaga, B. Dörling, A. Perevedentsev, J. Martín, J. S. Reparaz, and M. Campoy-Quiles, "Closing the Stability–Performance Gap in Organic Thermoelectrics by Adjusting the Partial to Integer Charge Transfer Ratio," *Macromolecules* 53 (2020): 609–620, https://doi.org/10.1021/acs.macromol.9b02263.

15. Y. Lu, J.-Y. Wang, and J. Pei, "Strategies to Enhance the Conductivity of n-Type Polymer Thermoelectric Materials," *Chemistry of Materials* 31 (2019): 6412–6423, https://doi.org/10.1021/acs.chemmater.9b01422.

16. H. Hase, K. O'Neill, J. Frisch, A. Opitz, N. Koch, and I. Salzmann, "Unraveling the Microstructure of Molecularly Doped Poly(3-hexylthiophene) by Thermally Induced Dedoping," *The Journal of Physical Chemistry C* 122 (2018): 25893–25899, https://doi.org/10.1021/acs.jpcc.8b08591.

17. J. Li, C. Koshnick, S. O. Diallo, et al., "Quantitative Measurements of the Temperature-Dependent Microscopic and Macroscopic Dynamics of a Molecular Dopant in a Conjugated Polymer," *Macromolecules* 50 (2017): 5476–5489, https://doi.org/10.1021/acs.macromol.7b00672.

18. E. H. Suh, S. B. Kim, J. Jung, and J. Jang, "Extremely Electron-Withdrawing Lewis-Paired CN Groups for Organic p-Dopants," *Angewandte Chemie International Edition* 62, no. 37 (2023): e202304245, https://doi.org/10.1002/anie.202304245.

19. I. Salzmann, G. Heimel, M. Oehzelt, S. Winkler, and N. Koch, "Molecular Electrical Doping of Organic Semiconductors: Fundamental Mechanisms and Emerging Dopant Design Rules," *Accounts of Chemical Research* 49 (2016): 370–378, https://doi.org/10.1021/acs.accounts.5b00438.

20. A. E. Mansour, R. Warren, D. Lungwitz, et al., "Coordination of Tetracyanoquinodimethane-Derivatives with Tris(pentafluorophenyl)Borane Provides Stronger p-Dopants with Enhanced Stability," *ACS Applied Materials & Interfaces* 15 (2023): 46148–46156, https://doi.org/10.1021/acsami.3c10373.

21. K. A. Peterson and M. L. Chabinyc, "Lewis Acid–Base Pair Doping of p-type Organic Semiconductors," *Journal of Materials Chemistry C* 10 (2022): 6287–6295, https://doi.org/10.1039/D2TC00605G.

22. D. T. Scholes, S. A. Hawks, P. Y. Yee, et al., "Overcoming Film Quality Issues for Conjugated Polymers Doped with F4TCNQ by Solution Sequential Processing: Hall Effect, Structural, and Optical Measurements," *The Journal of Physical Chemistry Letters* 6 (2015): 4786–4793, https://doi.org/10.1021/acs.jpclett.5b02332.

23. I. E. Jacobs, E. W. Aasen, J. L. Oliveira, et al., "Comparison of Solution-Mixed and Sequentially Processed P3HT:F4TCNQ Films: Effect of Doping-Induced Aggregation on Film Morphology," *Journal of Materials Chemistry C* 4 (2016): 3454–3466, https://doi.org/10.1039/C5TC04207K.

24. S. E. Yoon, Y. Kang, J. Im, et al., "Enhancing Dopant Diffusion for Ultrahigh Electrical Conductivity and Efficient Thermoelectric Conversion in Conjugated Polymers," *Joule* 7 (2023): 2291–2317, https://doi.org/10.1016/j.joule.2023.09.002.

25. S. B. Kim, S. Song, T. S. Lee, et al., "Influence of the Electronic Structures of Diketopyrrolopyrrole-Based Donor–Acceptor Conjugated Polymers on Thermoelectric Performance," *Journal of Materials Chemistry C* 12 (2024): 9227–9235, https://doi.org/10.1039/D4TC01568A.

26. C. Chen, I. E. Jacobs, K. Kang, et al., "Observation of Weak Counterion Size Dependence of Thermoelectric Transport in Ion Exchange Doped Conducting Polymers across a Wide Range of Conductivities," *Advanced Energy Materials* 13 (2023): 2202797, https://doi.org/10.1002/aenm.202202797.

27. J. Ding, Z. Liu, W. Zhao, et al., "Selenium-Substituted Diketopyrrolopyrrole Polymer for High-Performance p-Type Organic Thermoelectric Materials," *Angewandte Chemie International Edition* 58 (2019): 18994–18999, https://doi.org/10.1002/anie.201911058.

28. D. T. Scholes, P. Y. Yee, J. R. Lindemuth, et al., "The Effects of Crystallinity on Charge Transport and the Structure of Sequentially Processed F 4 TCNQ-Doped Conjugated Polymer Films," *Advanced Functional Materials* 27 (2017): 1702654, https://doi.org/10.1002/adfm.201702654.

29. I. E. Jacobs, J. Li, S. L. Burg, et al., "Reversible Optical Control of Conjugated Polymer Solubility with Sub-micrometer Resolution," *ACS Nano* 9 (2015): 1905–1912, https://doi.org/10.1021/nn506820d.

30. S. E. Yoon, J. M. Han, B. E. Seo, et al., "Optimized Selection of Dopant Solvents for Improving the Sequential Doping Efficiency of Conjugated Polymers," *Organic Electronics* 90 (2021): 106061, https://doi.org/10.1016/j.orgel.2021.106061.

31. J. Saska, G. Gonel, Z. I. Bedolla-Valdez, et al., "A Freely Soluble, High Electron Affinity Molecular Dopant for Solution Processing of Organic Semiconductors," *Chemistry of Materials* 31 (2019): 1500–1506, https://doi.org/10.1021/acs.chemmater.8b04150.

32. A. E. Laturski, J. R. Gaffen, P. Demay-Drouhard, C. B. Caputo, and T. Baumgartner, "Probing the Impact of Solvent on the Strength of Lewis Acids via Fluorescent Lewis Adducts," *Precision Chemistry* 1 (2023): 49–56, https://doi.org/10.1021/prechem.2c00009.

33. M. Heshmat and T. Privalov, "Carbonyl Activation by Borane Lewis Acid Complexation: Transition States of H_2 Splitting at the Activated Carbonyl Carbon Atom in a Lewis Basic Solvent and the Proton-Transfer Dynamics of the Boroalkoxide Intermediate," *Chemistry—A European Journal* 23 (2017): 9098–9113, https://doi.org/10.1002/chem.201700437.

34. O. Zapata-Arteaga, A. Perevedentsev, M. Prete, et al., "A Universal, Highly Stable Dopant System for Organic Semiconductors Based on Lewis-Paired Dopant Complexes," *ACS Energy Letters* 9 (2024): 3567–3577, https://doi.org/10.1021/acsenergylett.4c01278.

35. R. Lo, D. Manna, M. Lamanec, et al., "The Stability of Covalent Dative Bond Significantly Increases with Increasing Solvent Polarity," *Nature Communications* 13 (2022): 2107, https://doi.org/10.1038/s41467-022-29806-3.

36. R. Lo, D. Manna, V. M. Miriyala, D. Nachtigallová, and P. Hobza, "Trends in the Stability of Covalent Dative Bonds with Variable Solvent Polarity Depend on the Charge Transfer in the Lewis Electron-Pair System," *Physical Chemistry Chemical Physics* 25 (2023): 25961–25964, https://doi.org/10.1039/D3CP03445C.

37. Z. Yi, S. Wang, and Y. Liu, "Design of High-Mobility Diketopyrrolopyrrole-Based π-Conjugated Copolymers for Organic Thin-Film Transistors," *Advanced Materials* 27 (2015): 3589–3606, https://doi.org/10.1002/adma.201500401.

38. C. Wang, D. T. Duong, K. Vandewal, J. Rivnay, and A. Salleo, "Optical Measurement of Doping Efficiency in Poly(3-hexylthiophene) Solutions and Thin Films," *Physical Review B* 91 (2015): 085205, https://doi.org/10.1103/PhysRevB.91.085205.

39. I. H. Jung, C. T. Hong, U.-H. Lee, Y. H. Kang, K.-S. Jang, and S. Y. Cho, "High Thermoelectric Power Factor of a Diketopyrrolopyrrole-Based Low Bandgap Polymer via Finely Tuned Doping Engineering," *Scientific Reports* 7 (2017): 44704, https://doi.org/10.1038/srep44704.

40. J.-L. M. Abboud and R. Notari, "Critical Compilation of Scales of Solvent Parameters. Part I. Pure, Non-hydrogen Bond Donor Solvents," *Pure and Applied Chemistry* 71 (1999): 645–718, https://doi.org/10.1351/pac199971040645.

41. N. Y. Kim, T. S. Lee, D. Y. Lee, et al., "Enhanced Doping Efficiency and Thermoelectric Performance of Diketopyrrolopyrrole-Based Conjugated Polymers with Extended Thiophene Donors," *Journal of Materials Chemistry C* 9 (2021): 340–347, https://doi.org/10.1039/D0TC04094K.

42. H. Kim, S. B. Kim, S. Pyo, J. Jang, and I. H. Jung, "Distinctive Doping Behavior of Conjugated Polymers with Pendant-Side Conjugation for Enhanced Thermoelectric Properties," *Advanced Functional Materials* 35 (2025): 2422778, https://doi.org/10.1002/adfm.202422778.

43. T. L. Murrey, M. Berteau-Rainville, G. Gonel, et al., "Quantifying Polaron Densities in Sequentially Doped Conjugated Polymers: Exploring the Upper Limits of Molecular Doping and Conductivity," *Journal of Materials Chemistry C* 11 (2023): 14884–14895, https://doi.org/10.1039/D3TC01569F.

44. M. J. Friday, E. M. Kelley, A. Perez, D. H. Johnston, and C. M. Mauck, "DTT-DDQ Mixed-Stack Organic Charge-Transfer Crystals with Near-Infrared Absorption," *Crystal Growth & Design* 24 (2024): 9984–9993, https://doi.org/10.1021/acs.cgd.4c01156.

45. S. M. Whittemore and T. Autrey, "Kinetic and Thermodynamic Study of the Reduction of 1,1-Diphenylethylene by a Thermally Frustrated Diethyl Ether-BCF Lewis Pair," *Israel Journal of Chemistry* 55 (2015): 196–201, https://doi.org/10.1002/ijch.201400142.

46. I. Bányai, "Dynamic NMR for Coordination Chemistry," *New Journal of Chemistry* 42 (2018): 7569–7581, https://doi.org/10.1039/C8NJ00233A.

47. K.-J. Hwang, J.-S. Kim, K.-H. Cho, S.-G. Kong, and K. T. No, "The Influence of Dielectric Constant on Ionic and Non-polar Interactions," *Bulletin of the Korean Chemical Society* 24 (2003): 55–59.

48. O. Bubnova, Z. U. Khan, A. Malti, et al., "Optimization of the Thermoelectric Figure of Merit in the Conducting Polymer Poly(3,4-ethylenedioxythiophene)," *Nature Materials* 10 (2011): 429–433, https://doi.org/10.1038/nmat3012.

49. Y. Xu, W. Sun, Z. Chen, and J. Ouyang, "PEDOT:PSS Films with Very High Thermoelectric Properties through Water-Swollen Assisted Reduction with a Tetrakis(dimethylamino)Ethylene Solution," *Advanced Functional Materials* 34 (2024): 2410929, https://doi.org/10.1002/adfm.202410929.

50. D. R. Villalva, D. Derewjanko, Y. Zhang, et al., "Intermolecular-Force-Driven Anisotropy Breaks the Thermoelectric Trade-off in n-type Conjugated Polymers," *Nature Materials* 24 (2025): 1236–1244, https://doi.org/10.1038/s41563-025-02207-9.

51. O. Bubnova and X. Crispin, "Towards Polymer-Based Organic Thermoelectric Generators," *Energy & Environmental Science* 5 (2012): 9345, https://doi.org/10.1039/c2ee22777k.

52. E. H. Suh, S. B. Kim, H. S. Yang, and J. Jang, "Regulating Competitive Doping in Solution-Mixed Conjugated Polymers for Dramatically Improving Thermoelectric Properties," *Advanced Functional Materials* 32 (2022): 2207413, https://doi.org/10.1002/adfm.202207413.

53. E. H. Suh, J. G. Oh, J. Jung, S. H. Noh, T. S. Lee, and J. Jang, "Brønsted Acid Doping of P3HT with Largely Soluble Tris(pentafluorophenyl)borane for Highly Conductive and Stable Organic Thermoelectrics via One-Step Solution Mixing," *Advanced Energy Materials* 10 (2020): 2002521, https://doi.org/10.1002/aenm.202002521.

54. S. Wang, G. Zuo, J. Kim, and H. Sirringhaus, "Progress of Conjugated Polymers as Emerging Thermoelectric Materials," *Progress in Polymer Science* 129 (2022): 101548, https://doi.org/10.1016/j.progpolymsci.2022.101548.

55. H. Li, M. E. DeCoster, R. M. Ireland, J. Song, P. E. Hopkins, and H. E. Katz, “Modification of the Poly(bisdodecylquaterthiophene) Structure for High and Predominantly Nonionic Conductivity with Matched Dopants,” *Journal of the American Chemical Society* 139, no. 32 (2017): 11149–11157, https://doi.org/10.1021/jacs.7b05300.

56. H. Lee, L. Ayuningtias, H. Kim, et al., “From non-doped to dopable: The impact of methoxy functionalization on doping and thermoelectric properties of conjugated polymers,” *EcoMat* 6, no. 4 (2024), https://doi.org/10.1002/eom2.12442.

57. R. Kroon, D. Kiefer, D. Stegerer, L. Yu, M. Sommer, and C. Müller, “Polar Side Chains Enhance Processability, Electrical Conductivity, and Thermal Stability of a Molecularly p-Doped Polythiophene,” *Advanced Materials*, 29, no. 24 (2017): 1700930, https://doi.org/10.1002/adma.201700930.

58. V. Untilova, H. Zeng, P. Durand, L. Herrmann, N. Leclerc, and M. Brinkmann, “Intercalation and Ordering of F6TCNNQ and F4TCNQ Dopants in Regioregular Poly(3-hexylthiophene) Crystals: Impact on Anisotropic Thermoelectric Properties of Oriented Thin Films,” *Macromolecules* 54, no. 13 (2021): 6073–6084, https://doi.org/10.1021/acs.macromol.1c00554.

59. E. H. Suh, Y. J. Jeong, J. G. Oh, et al., “Doping of donor-acceptor polymers with long side chains via solution mixing for advancing thermoelectric properties,” *Nano Energy* 58 (2019): 585–595, https://doi.org/10.1016/j.nanoen.2019.01.075.

60. H. J. Cheon, T. S. Lee, J. E. Lee, et al., “Design of Donor–Acceptor Polymer Semiconductors for Optimizing Combinations with Dopants to Maximize Thermoelectric Performance,” *Chemistry of Materials* 35, no. 4 (2023): 1796–1805, https://doi.org/10.1021/acs.chemmater.2c03739.

61. D. Wang, J. Ding, Y. Ma, et al., “Multi-heterojunctioned Plastics with High Thermoelectric Figure of Merit,” *Nature* 632 (2024): 528–535, https://doi.org/10.1038/s41586-024-07724-2.

62. S. D. Kang and G. J. Snyder, “Charge-Transport Model for Conducting Polymers,” *Nature Materials* 16 (2017): 252–257, https://doi.org/10.1038/nmat4784.

63. Z. Liang, Y. Zhang, M. Souri, et al., “Influence of Dopant Size and Electron Affinity on the Electrical Conductivity and Thermoelectric Properties of a Series of Conjugated Polymers,” *Journal of Materials Chemistry A* 6 (2018): 16495–16505, https://doi.org/10.1039/C8TA05922E.

64. M. Jha, J. Mogollon Santiana, A. A. Jacob, et al., “Stability Study of Molecularly Doped Semiconducting Polymers,” *The Journal of Physical Chemistry C* 128 (2024): 1258–1266, https://doi.org/10.1021/acs.jpcc.3c06044.

65. C. Liu, D.-Y. Khim, and Y.-Y. Noh, “Organic Field-Effect Transistors by a Solvent Vapor Annealing Process,” *Journal of Nanoscience and Nanotechnology* 14 (2014): 1476–1493, https://doi.org/10.1166/jnn.2014.9101.

66. T. J. Aubry, K. J. Winchell, C. Z. Salamat, et al., “Tunable Dopants with Intrinsic Counterion Separation Reveal the Effects of Electron Affinity on Dopant Intercalation and Free Carrier Production in Sequentially Doped Conjugated Polymer Films,” *Advanced Functional Materials* 30 (2020): 2001800, https://doi.org/10.1002/adfm.202001800.

67. J. L. Bredas and G. B. Street, “Polarons, Bipolarons, and Solitons in Conducting Polymers,” *Accounts of Chemical Research* 18 (1985): 309–315, https://doi.org/10.1021/ar00118a005.

68. D. T. Duong, C. Wang, E. Antono, M. F. Toney, and A. Salleo, “The Chemical and Structural Origin of Efficient p-type Doping in P3HT,” *Organic Electronics* 14 (2013): 1330–1336, https://doi.org/10.1016/j.orgel.2013.02.028.

69. S. Wood, J. Wade, M. Shahid, et al., “Natures of Optical Absorption Transitions and Excitation Energy Dependent Photostability of Diketopyrrolopyrrole (DPP)-Based Photovoltaic Copolymers,” *Energy & Environmental Science* 8 (2015): 3222–3232, https://doi.org/10.1039/C5EE01974E.

70. J. Terao, A. Wadahama, A. Matono, et al., “Design Principle for Increasing Charge Mobility of π-conjugated Polymers Using Regularly Localized Molecular Orbitals,” *Nature Communications* 4 (2013): 1691, https://doi.org/10.1038/ncomms2707.

71. R. Ghosh, C. K. Luscombe, M. Hambsch, S. C. B. Mannsfeld, A. Salleo, and F. C. Spano, “Anisotropic Polaron Delocalization in Conjugated Homopolymers and Donor–Acceptor Copolymers,” *Chemistry of Materials* 31 (2019): 7033–7045, https://doi.org/10.1021/acs.chemmater.9b01704.

72. S. A. Gregory, R. Hanus, A. Atassi, et al., “Quantifying Charge Carrier Localization in Chemically Doped Semiconducting Polymers,” *Nature Materials* 20 (2021): 1414–1421, https://doi.org/10.1038/s41563-021-01008-0.

73. M. K. Ourgessa, J. R. McClellan, D. H. Johnston, and C. M. Mauck, “Molecular p-Doping in Thiophene Diketopyrrolopyrrole Thin Films through Formation of a Charge Transfer Complex,” *The Journal of Physical Chemistry C* 127 (2023): 18694–18705, https://doi.org/10.1021/acs.jpcc.3c03912.

74. A. J. Wise and J. K. Grey, “Resonance Raman Studies of Excited State Structural Displacements of Conjugated Polymers in Donor/Acceptor Charge Transfer Complexes,” *Physical Chemistry Chemical Physics* 14 (2012): 11273, https://doi.org/10.1039/c2cp41748k.

75. P. Panda, D. Veldman, J. Sweelssen, J. J. A. M. Bastiaansen, B. M. W. Langeveld-Voss, and S. C. J. Meskers, “Charge Transfer Absorption for π-Conjugated Polymers and Oligomers Mixed with Electron Acceptors,” *The Journal of Physical Chemistry B* 111 (2007): 5076–5081, https://doi.org/10.1021/jp070796p.

76. I. McCulloch, M. Heeney, C. Bailey, et al., “Liquid-Crystalline Semiconducting Polymers with High Charge-Carrier Mobility,” *Nature Materials* 5 (2006): 328–333, https://doi.org/10.1038/nmat1612.

77. S. Ueji, M. Sugiura, and N. Takao, “Aromatic Solvent-Induced Shifts (ASIS) in Carbon-13 NMR Spectroscopy,” *Tetrahedron Letters* 21 (1980): 475–478, https://doi.org/10.1016/S0040-4039(00)71437-7.

78. G. L. Nelson, G. C. Levy, and J. D. Cargioli, “Solvent Effects in Carbon-13 Nuclear Magnetic Resonance. Electronic Perturbation of Aromatic Systems,” *Journal of the American Chemical Society* 94 (1972): 3089–3094, https://doi.org/10.1021/ja00764a033.

Supporting Information

Additional supporting information can be found online in the Supporting Information section.

Supporting File: adma72913-sup-0001-SuppMat.docx.